In situ XAFS experiments using a microfluidic cell: application to initial growth of CdSe nanocrystals

H. Oyanagi,[a,b]* Z. H. Sun,[a,b]‡ Y. Jiang,[a,b] M. Uehara,[c] H. Nakamura,[c] K. Yamashita,[c] L. Zhang,[c] C. Lee,[c] A. Fukano[a]¶ and H. Maeda[c,d,e]

[a]Photonics Research Institute, National Institute of Advanced Science and Technology, 1-1-1 Umezono, Tsukuba, Ibaraki 305-8568, Japan, [b]National Synchrotron Radiation Laboratory, University of Science and Technology of China, Hefei, Anhui 230029, People's Republic of China, [c]Measurement Solution Research Center, National Institute of Advanced Industrial Science and Technology, 807-1 Shuku-machi, Tosu, Saga 841-0052, Japan, [d]Department of Molecular and Material Sciences, Interdisciplinary Graduate School of Engineering Sciences, Kyushu University, 6-1 Kasuga-koen, Kasuga, Fukuoka 816-8580, Japan, and [e]CREST, Japan Science and Technology Agency, 4-1-8 Hon-chou, Kawaguchi, Saitama 332-0012, Japan. E-mail: h.oyanagi@aist.go.jp

The design and performance of a compact fluorescense XAFS apparatus equipped with a microfluidic cell for *in situ* studies of nanoparticles are described. CdSe nanoparticles were prepared by solution reaction starting from trioctylphosphine-Se. Time-resolved experiments were performed by precisely controlling the reactor coordinates (x,y), allowing the synchrotron X-ray beam to travel along a reactor channel, covering nucleation and initial growth of nanoparticles. Detailed analysis of EXAFS data combined with UV–vis spectra allow reliable estimation of particle size and density in the initial growth that cannot be accessible by conventional optical techniques based on a long-range order. The Se K-XANES spectra are interpreted by multi-scattering calculations providing bond formation kinetics consistent with the EXAFS data.

Keywords: XAFS; EXAFS; XANES; microfluidic cell; CdSe nanocrystal.

1. Introduction

The past two decades have witnessed an explosive expansion of research on semiconductor nanoparticles (NPs) owing to their size-dependent properties and applications in a variety of fields such as solar cells, light-emitting diodes and biological imaging (Alivisatos, 1996; Rosenthal *et al.*, 2007; Park *et al.*, 2007). To synthesize these NPs with desired size and shape and thus to tailor their structural and physical properties, understanding of the nucleation and growth processes is of essential importance (Park *et al.*, 2007). In most cases the nucleation is described by the classical nucleation theory (CNT) (Laaksonen *et al.*, 1995), which assumes the same structure of nuclei as that of the stable NPs. NPs grown from these nuclei can be monitored by transmission electron microscopy (TEM) or optical spectra, such as UV–vis absorption and photoluminescence (PL). Among these methods, UV–vis absorption is the most convenient and practical (Yu *et al.*, 2003), and the appearance of excitonic absorption peaks serves as a fingerprint of the formation of crystallized NPs. However, optical spectra provide little information during the time region when

no optical absorption features are observed. So far, a few theoretical (Moroni *et al.*, 2005; Doye & Calvo, 2001) and experimental studies (Zhang & Liu, 2007, 2009) have challenged the CNT, and in some cases it is found that the initial nuclei are not in an ordered state (Zhang & Liu, 2007, 2009), making them even more difficult to be observed using optical spectra. Since the nucleation strongly influences the subsequent growth process varying from system to system, detailed knowledge about nucleation is needed for each specific system.

On the other hand, it has been recognized that the size growth of NPs occurs simultaneously with the crystallization process involving structural reconstruction and surface relaxations (Leung & Whaley, 1999; Zhang *et al.*, 2002; McGinley *et al.*, 2002). Generally, the excitonic peak of UV–vis absorption spectra red-shifts over time, reflecting the size change. This picture has been the basis of numerous studies on the growth kinetics of nanocrystals (NCs) in the literature (Bullen & Mulvaney, 2004; Nakamura *et al.*, 2002; Xie *et al.*, 2008). However, the use of UV–vis absorption neglects the possible non-crystalline structures (Piepenbrock *et al.*, 2007). Hence, previous kinetic studies of the growth of CdS, CdSe and CdTe NPs based on optical spectra using Yu *et al.*'s calibration curve (Yu *et al.*, 2003) are actually limited to the crystallized part, disregarding the growth path through an

amorphous phase. In fact, the existence of amorphous CdSe NPs and their gradual crystallization has been confirmed experimentally (Epifani *et al.*, 2008; Chen *et al.*, 2005), especially for the particles grown at relatively low temperature.

Without a long-range order, the features in optical spectra would be smeared out and obscured by those from the crystalline particles like in the case of X-ray diffraction (XRD). The amorphous state with defects could be reflected by the extrinsic features involving surface defects states in the UV–vis absorption spectra (Leung & Whaley, 1999) or by the trap-state emission in photoluminescence (PL) spectra (Soloviev *et al.*, 2000), but unfortunately these extrinsic features are always very weak and their interpretations are ambiguous. High-resolution TEM (HRTEM) is a direct method of observing nanostructures, but it is difficult to observe ultra-small amorphous particles owing to a few problems such as low phase contrast between the amorphous material and carbon support (Rosenthal *et al.*, 2007), complicated sample treatment, and electron beam radiation-induced crystallization (Epifani *et al.*, 2008). Owing to these reasons and to the short observation time window for the amorphous NPs, investigations on the simultaneous crystallization and growth processes have not been performed, leading to limited works that reported the separated crystallization process (Epifani *et al.*, 2008; Chen *et al.*, 2005).

In this work we describe the combination of optical spectra and *in situ* X-ray absorption fine structure (XAFS) techniques including extended-XAFS (EXAFS) and X-ray absorption near-edge structure (XANES), to study the simultaneous growth and crystallization of CdSe NPs synthesized in a microfluidic reactor (Uehara *et al.*, 2009). The use of a microfluidic reactor allows for the independent and accurate control of the reaction parameters, such as temperature, reaction time and precursor concentrations in a reproducible way (Nakamura *et al.*, 2002, 2004; Yen *et al.*, 2003). The use of *in situ* XAFS measurements enables us to study the bond formation kinetics, monitoring the growth process of the total CdSe particles, including the crystallized and amorphous phases. Since crystallized particles will be detected by UV–vis absorption and PL spectra, the combination allows us to observe the gradual crystallization associated with particle size increase as the reaction proceeds.
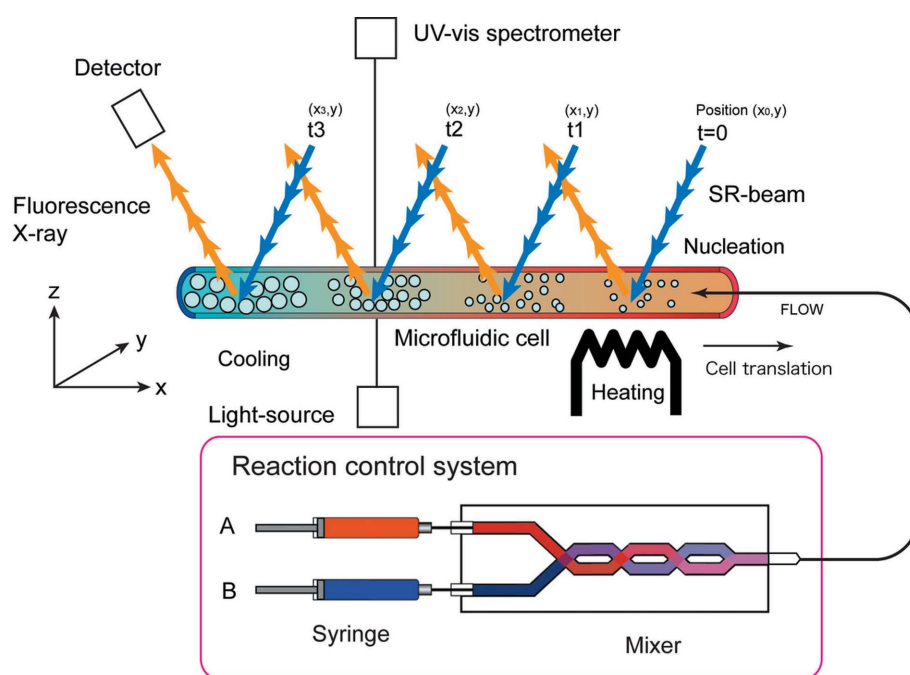
2. Experimental set-up

2.1. Microfluidic cell

Recently, controlled synthesis using microfluidic systems has attracted attention in various fields such as organic and inorganic chemistry,

biology and medicine (Yoshida, 2003; Geyer *et al.*, 2006; Sahoo *et al.*, 2007). The microfluidic systems allow for rapid mass and thermal transfer, and provide an ideal medium for NP synthesis, specifically with respect to kinetic control. A special feature of a microfluidic system is its ability to independently control parameters (*e.g.* reaction time, temperature and concentration) in a precise and reproducible manner. Various kinds of continuous-flow cells are used to study short-lived reaction intermediates or for reducing radiation damage while avoiding the artifacts associated with freezing owing to ice crystals (Tsuruta *et al.*, 1989; Kihara, 1994). In the stopped-flow studies a rapid spectroscopy measurement was performed for a closed cell after chemical or biological reactions were abruptly terminated. The first application of a microfluidic cell to synchrotron radiation research (Chan *et al.*, 2007) used a microbeam to observe a cation exchange reaction *in situ*. Here we describe the *in situ* XAS set-up using a more general focused undulator X-ray beam [1 mm (H) × 0.5 mm (V)], matching the typical size of a flow cell (500 µm) originally designed for initial growth study of CdSe NPs (Nakamura *et al.*, 2002).

Fig. 1 schematically illustrates the principle of the experimental set-up. The basic idea is to measure time-dependent XAFS by means of position-dependence independently recorded at different positions along a laminar flow. Figs. 2(*a*) and 2(*b*) show the planar and side views of the set-up, respectively. By changing the position of the microfluidic cell on a computer-controlled high-precision XY-stage, position-dependent XAFS spectra are recorded in a fluorescence detection mode moving along a reactor channel. Several reactor channel (planar) designs are illustrated in Fig. 2(*c*).
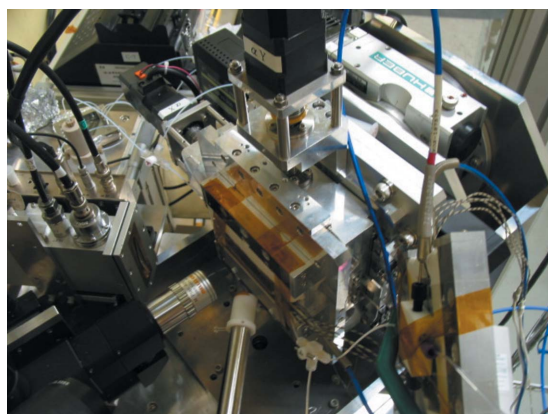

Figure 1
Schematic principle of the *in situ* XAFS experimental set-up using a microfluidic cell. Fluorescence yield spectra recorded at positions (x, y) along a microreactor channel provide time-dependent XAFS spectra. In the present reaction, precursor flows (TOP-Se and Cd stock solution) are mixed before introducing to a heated microchannel.
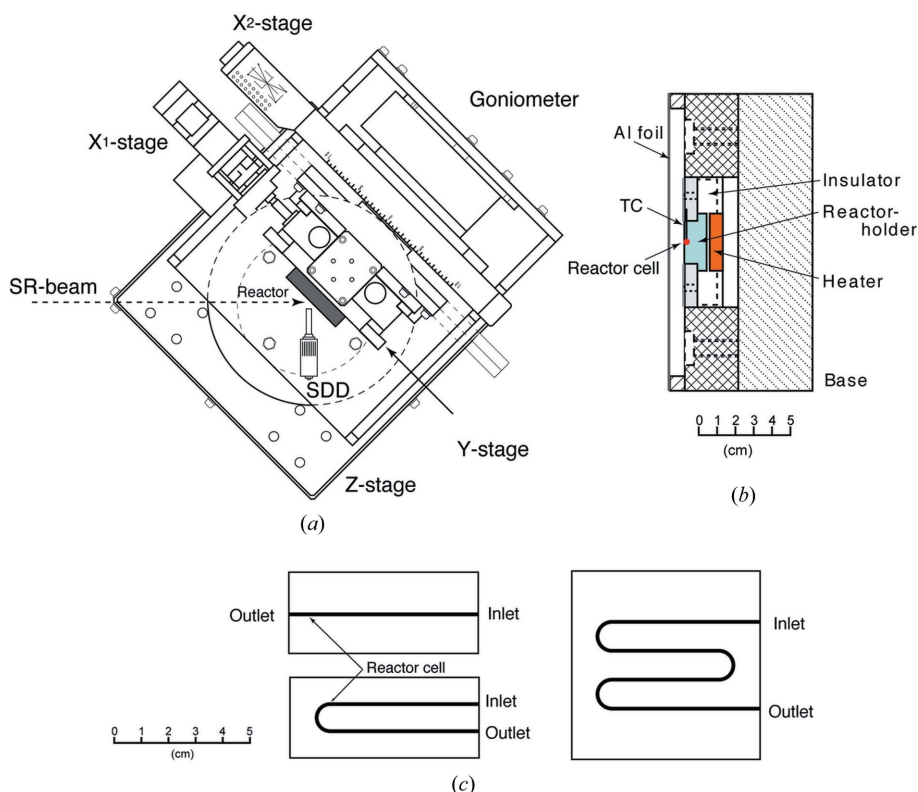
Figure 2
(a) Plan view of the *in situ* XAFS apparatus equipped with a microfluidic cell. (b) Side view of the microfluidic cell mounted on an aluminium baseplate. (c) Different channel designs covering a wide reactor length (80–300 mm).

Depending on the required reactor channel length that determines the observing time window, the suitable reactor subassembly is determined and mounted on the XY-stage. Fig. 3 shows a photograph of the experimental set-up around the reactor mounted on the XY-stage. The temperature distribution of the reactor channel is monitored in real time by an IR-TV camera [JENOPTIK Laser, Optik Systeme GmbH,

Vario CAM(R) HiRes]. Fig. 4 shows the distribution of temperature along the U-shaped flow channels, where one can find an abrupt temperature rise near the flow inlet and a constant temperature distribution extending along the rest of channel. As can be seen, the temperature distribution is sensitive to the velocity and mass of the flow.

The experimental details on the synthesis of CdSe NPs (Uehara *et al.*, 2009; Sun *et al.*, 2010) are briefly described here. Three raw-material stock solutions [Se source, Cd source and dodecylamine (DDA) ligand solutions] were prepared. The selenium stock solution (TOP-Se) was prepared by dissolving selenium powder in tri-octylphosphine (TOP) and then diluted in octadecene (ODE), a non-coordinating solution. The cadmium stock solution was prepared by heating a mixture of $Cd(CH_3COO)_2 \cdot 2H_2O$, oleic acid and ODE at 453 K under Ar flow. The DDA solution was prepared by dissolving DDA in ODE. These stock solutions were loaded into glass syringes separately and then mixed in a mixer connected to a capillary KAPTON tube with an inner diameter of 0.5 mm.

Several reactor channel materials such as TEFLON, KAPTON and glass were tested and compared in terms of radiation damage and precipitation on the tube surface. A 70 cm length of the capillary tube was attached to the heating unit, where the mixed solution injected at a constant velocity of 7.6 mm s^{-1} was heated to a target temperature of 513 K. In the mixed solution the Se and Cd concentrations were kept at 30 and 12 mM, respectively, and the DDA concentration varied from 5 to 10 wt%.
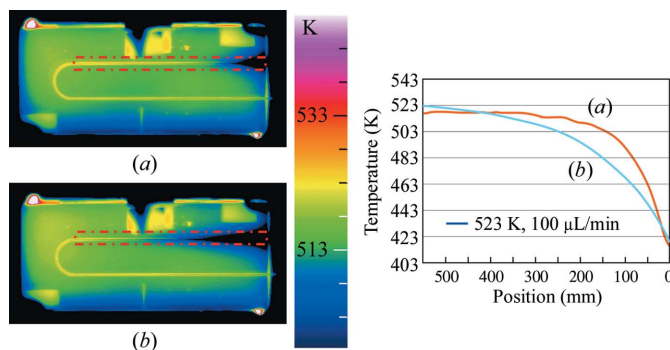

Figure 3
Photograph showing the *in situ* XAFS apparatus equipped with a microfluidic cell. The incident beam intensity is monitored by an ion chamber in front of a reactor. A silicon drift diode detector is used to record the fluorescence signal. The temperature distribution and optical image of a heated reactor channel is monitored by an IR-TV camera and a telescopic TV camera, respectively.

Figure 4
Temperature distribution of the microfluidic cell and baseplate measured using an IR-TV. Positions correspond to elapsed time (0–8.1 s) as measured from a starting position for a U-shaped reactor channel where (a) and (b) denote the results for an octadecene flow speed of 100 µL min^{-1} (8.5 mm s^{-1}) and 250 µL min^{-1} (21.2 mm s^{-1}), respectively.

2.2. XAS measurement

In situ EXAFS measurements at the Se *K*-edge were performed initially at multipole wiggler (MPW) beamline BL13B1 of the Photon Factory (PF) and later at NW2 (X-ray tunable undulator) of the Advanced Ring for Pulsed X-rays (PF-AR) of the High Energy Accelerator Research Organization, Japan. The reactor KAPTON tube is embedded in a thermal insulator and mounted on an aluminium holder (Fig. 2*c*). Experiments at a MPW beamline allow us to study various *K*-edges that spread wide in energy, while an undulator beam is advantageous as it is optimized in dimension to the reactor. We note that both glass and KAPTON materials were resistive to radiation damage in the hard X-ray region (~11 keV) while TEFLON quickly deteriorates with the high-flux (NW2 focused undulator) beam, although the latter has superior characteristics against precipitation on the tube wall. The linear microfluidic cell is mounted on a stepping-motor-controlled XY-stage which rotates around the goniometer whose rotating axis is perpendicular to the stage normal, allowing either horizontal or vertical arrangements. Our standard reactor mounting is horizontal whereas a vertical mounting is designed for moving the reactor channel in order to prevent precipitation and radiation damage of the tube material. We have developed a high-precision XY-stage (denoted as X_1, Y) with a stroke of 40 mm for each axis. To extend the stroke along the *x*-axis, the main XY stage is mounted on a commercial 200 mm stroke X stage [SGSP-33-200(X), Sigma Koki] denoted as X_2. Each axis is driven by a five-phase stepping motor. The reactor position described by the coordinates (X_1, X_2, Y) is controlled by software on a linux-PC, allowing us to align an incident beam position within an area of 40 mm × 80 mm on the reactor surface with 1 μm precision. The software controls the (X_1, X_2, Y) coordinates *via* a LAN-based stepping-motor controller (Laboratory Equipment NT2400).

The energy resolution was better than 2 eV at 9 keV, calibrated from the near-edge features of copper metal at E_f (8.9803 keV). For each DDA concentration a series of EXAFS data, corresponding to reaction times of 0.0, 1.1, 1.4, 1.8, 2.4, 3.0, 5.0 and 8.1 s, was collected (Sun *et al.*, 2010). Under the same reaction conditions as in the *in situ* EXAFS experiment, *ex situ* UV–vis absorption and PL spectra were measured using a UV–vis spectro-photometer (QE65000; Ocean Optics, USA). PL spectra were measured at an excitation wavelength of 365 nm. The optical spectrophotometers were

attached to a glass tube with an inner diameter of 0.5 mm connected to the outlet of the reactor tube (Nakamura *et al.*, 2002). The typical intensity of the fluorescence signal for Se-TOP exceeds 50–60 kcounts s^{-1} above the Se *K*-edge but we measured the intensity at a safe limit (around 30 kcounts s^{-1}) to minimize the dead-time correction using an Amptek PX4 digital signal processor. Early studies used a compact silicon drift diode (SDD) detector, Amptek XR-100SDD (9 mm^2; Amptek), which was replaced by a Vortex EX-90 (50 mm^2, SEIKO EG&G) in later stages.

3. Results and discussion

3.1. Bond formation kinetics

The temporal evolutions of the UV–vis absorption and PL spectra of the CdSe NPs are shown in Fig. 5. Stability of the flow is demonstrated by the time-dependence of spectral intensities measured at several wavelength values. Evidently, the absorption and luminescence curves are featureless within the first 2.4 s of the reaction. As the reaction time proceeded to 2.4 s or longer, excitonic absorption and PL peaks appear, with the intensities and peak positions increasing rapidly with time. The appearance of these absorption and emission peaks indicates the formation of crystalline CdSe NPs, and the
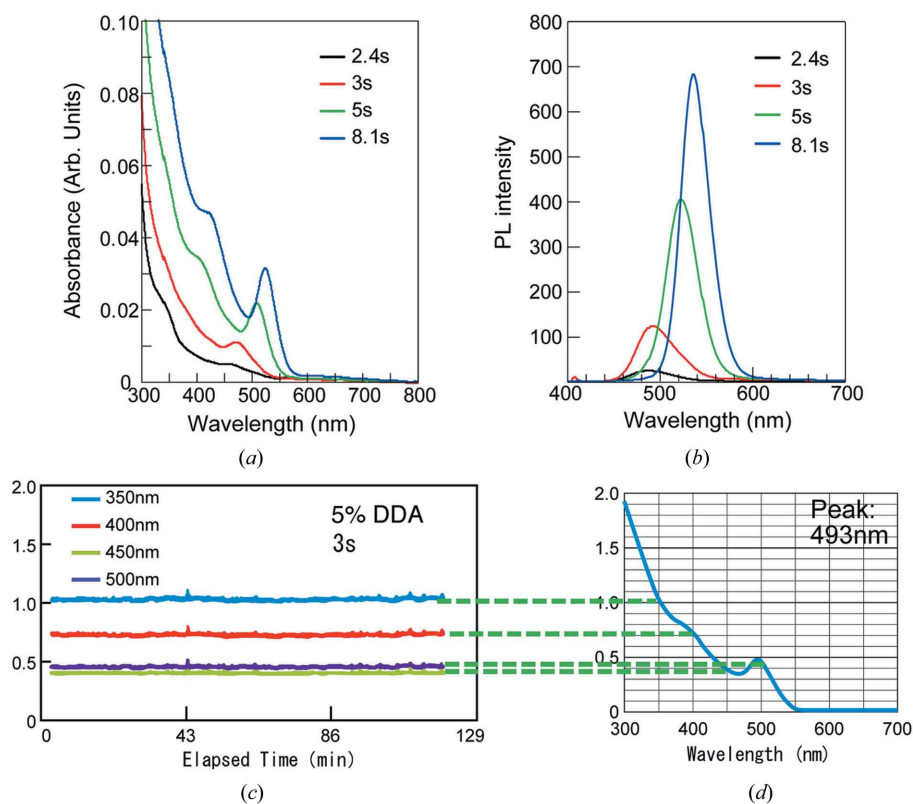
Figure 5
(*a*) UV–vis absorbance spectra of the CdSe NPs in the presence of 5 wt% DDA. (*b*) PL spectra of the CdSe NPs for the same solution. The spectra were normalized with respect to the PL intensity at 8.1 s. (*c*) Stability of products (CdSe NPs) (3 s) recorded as intensity variations of specific spectral features in the UV–vis spectra (*d*) as a function of elapsed time. The time scale of fluctuation is much shorter than the integration time (4 s) which averages out the variation.
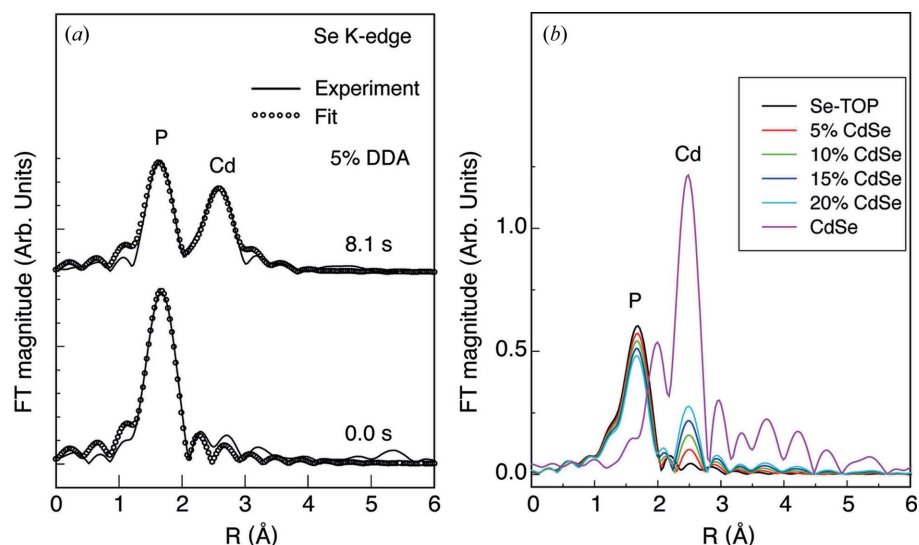
Figure 6
(a) Magnitude of the Fourier transform (FT) of the k^2-weighted experimental EXAFS data measured with elapsed time in seconds. Solid lines represent the experimental data (Sun *et al.*, 2009) and open circles show the fitting results. (b) FT magnitude of the k^2-weighted EXAFS simulation for a two-component model with various compositions of CdSe together with reference CdSe and Se-TOP.

gradual red-shift of the peaks displays their size growth. The full width at half-maximum (FWHM) of the PL peak in the presence of 5 wt% DDA decreases continuously from 53 nm at 2.4 s to 35 nm at 8.1 s, indicating the size focusing of the crystalline particles accompanied with size growth. However, no obvious size focusing of the crystalline NPs can be inferred for the 10 wt% DDA case, because the FWHM in the PL spectra keeps above 50 nm within the time range 2.4–8.1 s and does not reduce with time. The absence of any visible UV–vis absorption peak in the wavelength range 350–450 nm rules out the possibility of the existence of magic size clusters (Wang *et al.*, 2004; Jose *et al.*, 2006; Kudera *et al.*, 2007), which are known to be stable only at relatively low temperatures of 363–423 K (Wang *et al.*, 2004). Using the absorbance intensity at a wavelength of 350 nm (Nakamura *et al.*, 2004) and the FWHM of the PL spectrum (Yu *et al.*, 2003), the reaction yield of Se, the average size and concentration of the NCs were estimated.

The EXAFS data analysis procedure and fitting strategy were identical to those adopted in our previous paper (Sun *et al.*, 2010). The oscillation functions were extracted from the raw experimental spectra using the *ATHENA* module (Ravel & Newville, 2005), and the least-squares parameter fitting was performed using the *ARTEMIS* module (Ravel & Newville, 2005). Both modules are implemented in the *IFEFFIT* package (Newville, 2001). The solid lines in Fig. 6(a) show the Fourier transform (FT) magnitudes of the k^2-weighted $\chi(k)$ functions using a Hanning window and a k-range of 2.5–10.5 Å^{-1} for t = 0.0 and 8.1 s. At the starting time t = 0.0 s, only a prominent peak at 1.6 Å ascribed to the Se—P bond of TOP-Se is visible for both DDA concentrations (5% and 10%), which resembles the spectral shape of the starting material TOP-Se. After that a peak at 2.5 Å attributed to the Se—Cd bonds becomes apparent at the reaction time of 8.1 s. This observation is strikingly different from those using optical

spectra, which indicated the formation of CdSe NCs only after 2.4 s of the reaction. Upon further increasing the reaction time, the Se—Cd peak intensity is enhanced and, at the same time, the Se—P peak intensity decreases gradually. Furthermore, it is noticeable that the Se—Cd peak intensity increase (and the Se—P peak intensity decrease) is quicker when the added DDA concentration is higher. This implies that higher DDA concentration facilitated the conversion of TOP-Se into CdSe particles. Systematic intensity variation of the FT magnitude for simulated EXAFS oscillations (Fig. 6b) clearly indicates good correlation of the two components, *i.e.* Se—Cd and Se—P pairs (Sun *et al.*, 2009).

Least-squares parameter fitting was performed to extract quantitative results using the same fitting strategy as described in detail in our previous paper (Sun *et al.*, 2010). An adjustable parameter Y referring to the percentage of Se in CdSe particles was refined in the fitting which actually denotes the reaction yield of Se. The obtained bond lengths ($R_{Se–P}$ = 2.11–2.13 ± 0.02 Å, $R_{Se–Cd}$ = 2.59–2.63 ± 0.04 Å) did not show obvious time-dependence within the error bars.

3.2. Formation of amorphous nanoparticles

The formation of CdSe particles observed by EXAFS at 1.1 s (Sun *et al.*, 2009) is confirmed by UV–vis absorption after 2.4 s (Fig. 5b). Such discrepancy is explained by the formation of amorphous NPs. For amorphous CdSe particles, no excitonic feature in UV–vis absorption spectra can be observed (Epifani *et al.*, 2008), but the Se—Cd peak in EXAFS persists. The size distribution of these amorphous particles might be as wide as that of their crystalline counterpart. Moreover, the presence of amorphous NPs is consistent with the PL measurements (Fig. 5). The PL of nanoparticles is contributed to by the band-gap emission (Bowers *et al.*, 2005) and the trap-state emission (Soloviev *et al.*, 2000). The band-gap PL is slightly shifted from the absorption onset and its FWHM is an indicator of the size distribution of the particles (Yu *et al.*, 2003). The trap-state PL, originating from the emission of deep-trap states with relatively low density of states (Schreuder *et al.*, 2009), is substantially red-shifted from the absorption onset (Chen *et al.*, 2005; Zhao *et al.*, 1999; McIlroy *et al.*, 1999; Persans *et al.*, 2000), resulting in a long tail of the band-gap PL. Such a long tail can really be observed in the PL spectra at 2.4 and 3.0 s for the 5 wt% DDA case. With increasing reaction time the long tail gradually disappears and the PL spectra become symmetric in shape and the peak is narrowed. This phenomenon may be explained by the removal
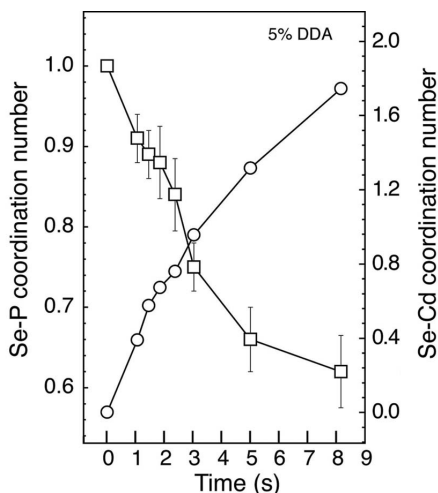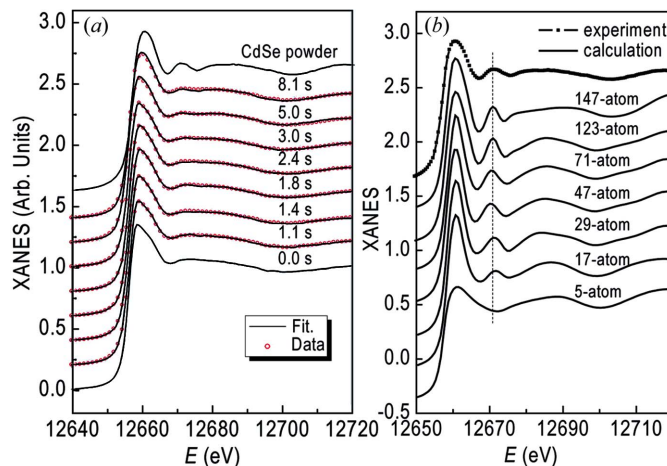
Figure 7
Experimentally determined Se−P coordination number (squares) and Se−Cd coordination number (circles) measured at various elapsed times.
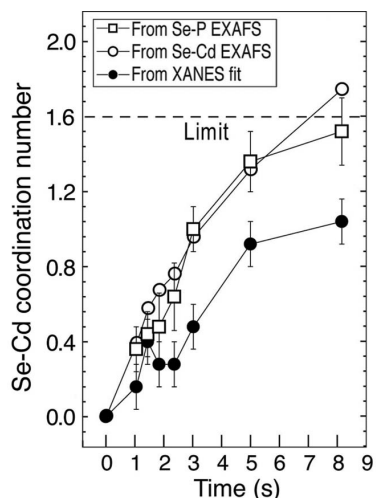

Figure 8
(a) Experimental and simulated XANES spectra measured at various positions corresponding to the elapsed time after initiation of the reaction with the addition of 5 wt% DDA, together with reference spectra for CdSe powder crystals and CdSe nanocrystals with an average diameter of 3 nm. Open circles indicate simulated XANES spectra. (b) Size-dependent XANES calculations for a wurtzite-structured CdSe cluster. The structural model of the CdSe cluster including five atoms is composed of the central Se atom and four first-shell Cd neighbors with their relative positions identical to that in the wurtzite CdSe crystal. Each subsequent calculation includes the next coordination shell around the central Se into the cluster. For example, the 17-atom cluster consists of the central Se, four first-shell Cd atoms and 12 second-shell Se atoms and so on. The calculation converges for a 147-atom cluster. Even for the 17-atom cluster the calculated XANES can produce most of the experimental features.

of the initial deep-trap surface states through gradual crystallization of the amorphous particles.

The NC size increase with time demonstrates the simultaneous occurrence of growth and crystallization of CdSe NPs under current reaction conditions (Fig. 7). In the presence of 10 wt% DDA the percentage of crystalline particles is below 10% within the first 3 s of the reaction, implying the dominant existence of amorphous nuclei in the initial reaction stage. This observation is in agreement with previous theoretical (Moroni *et al.*, 2005; Doye & Calvo, 2001) and experimental studies (Zhang & Liu, 2007, 2009) that the initial nuclei are disordered, contrary to the CNT assuming the same structure of nuclei as that of the stable NPs (Rosenthal *et al.*, 2007). From the viewpoint of the energy-configuration curve, the amorphous particles are located at a local minimum and the stable crystalline particles are represented by a global minimum (Epifani *et al.*, 2008). There is an energy barrier in the crystallization process which can be overcome either dynamically (*e.g.* at high temperature) or kinetically (*e.g.* at long growth time). For NPs grown at elevated temperature or with long reaction time the crystallinity would be improved.

3.3. XANES spectra compared with multiple-scattering calculations

The XANES spectra shown in Fig. 8(*a*) can be used as an alternative means of providing bond formation kinetics but the data contain more three-dimensional atomic arrangements and can provide useful information on the structure distinguishing similar radial distribution functions. Before fitting experimental XANES with a two-component model, we tested the cluster size dependence using the *ab initio* multiple-scattering code *FEFF8.20* (Ankudinov *et al.*, 2002). The validity of our (two-component) model was confirmed by the EXAFS simulation (Fig. 6*b*) and XANES simulation that shows an isosbestic point (not shown). Fig. 8(*b*) shows the calculated XANES spectra for a different cluster size compared with the experimental data for a wurtzite-structured CdSe cluster. The

results demonstrate that the XANES for the five-atom cluster is different from that of a 17-atom cluster and beyond that the characteristic peak (indicated by the vertical dashed line) of wurtzite CdSe is missing. This shows the ability of Se *K*-edge XANES to distinguish the wurtzite-structured CdSe and small CdSe clusters consisting of only a few atoms. For instance, in smaller clusters such as $(CdSe)_3$ the Se−Cd bond length is close to 2.63 Å (Jose *et al.*, 2006), but their XANES spectra would be distinct from that of wurtzite structure.

Fig. 8(*a*) shows that the experimental XANES gradually changes from that of the starting material TOP-Se to the spectrum of wurtzite-type CdSe, and can be fitted through a linear combination of the standard spectra of TOP-Se and CdSe powder. Thus, from the independent measurement of XANES and EXAFS, one can obtain the kinetics information independently making the fitting results reliable and informative. The use of a two-component model is justified by the fact that the selenium species do not form long-lived intermediates or stay as surplus ions without forming bonds. However, the CdSe product NPs have surface dangling bonds or bonds with surfactant (DDA) and this surface effect should be taken into account in the case of small cluster size. In our calculations the surface effect is neglected as we consider relatively large size clusters.

3.4. Estimation of CdSe formation yield

The difficulty in *in situ* data analysis is related to a general problem in the analysis of multiphases. Although both

Figure 9
Se—Cd coordination number as a function of elapsed time determined by EXAFS independently for the Se—P and Se—Cd pairs (open squares and open circles, respectively) compared with the value determined by the XANES fit (closed circles). The dashed line indicates the Se—Cd coordination limit. The reacted amount of Se and Cd during the reaction is assumed to be equal. As the initial [Se] and [Cd] concentrations are 30 mM and 12 mM, respectively, the upper limit of the reaction yield is $[Cd]_0/[Se]_0 = 40\%$.

EXAFS and XANES fits can estimate the CdSe formation yield y as a function of elapsed time t, there remain some critical issues that may lead to significant error. Fig. 9 shows a least-squares curve fit analysis of EXAFS oscillations which estimates the elapsed time-dependent coordination numbers for the Se—P and Se—Cd pairs (Sun *et al.*, 2009) compared with XANES results (present work). Product CdSe NPs (with a tetrahedral local structure) independently estimated from the Se—P and Se—Cd peaks were quantitatively consistent indicating that a two-component model is valid, *i.e.* unreacted Se-TOP does not dissolve leaving Se^{2-} ions. In general, however, the third component (if present) would interfere with the other two components in the first-shell region (1–3 Å) of the FT, causing significant error in the coordination number. Although the overall trend of bond formation kinetics describes the reaction kinetics (Sun *et al.*, 2009), significant error is found in the Se—Cd coordination number at $t = 8.1$ s, where precipitation of Se(0) onto the reactor wall is present. These results indicate that conventional EXAFS analysis overestimates the reaction yield with the presence of precipitation onto the tube wall. In order to avoid the possibility of precipitation, careful monitoring of the fluorescence signal intensity after each scan is required.

In contrast, estimation of the reaction yield by XANES fit is sensitive to the choice of the reference. Although we used CdSe NC (3 nm) carefully prepared in the laboratory under the same reaction conditions and characterized by UV–vis spectroscopy, the analysis systematically underestimates the reaction yield as illustrated in Fig. 9, suggesting difficulty in reproducing the properties (size and structural relaxation) of NCs off-line. Several possibilities of discrepancy between the two methods were examined. In general, XANES features are sensitively influenced by interference owing to multiphases

through multiple-scattering events, while in EXAFS the nearest-neighbor shell (single-scattering event) is affected less, particularly when the third phase does not give sharp peaks in the FT. Secondly, a most crucial issue is the appropriateness of the reference with respect to (i) NP size, (ii) disorder and (iii) temperature effects (thermal vibrations), all of which would smear out near-edge spectral features, leading to underestimation of yield. In the present case, although the reference was chosen to be close to the product NP, a significant underestimation was caused by (ii) and (iii). Indeed, the observed size (2–2.6 nm) was smaller than the reference (3 nm) and reference data were recorded at room temperature. We also need to take surface effects (structural relaxation) into account. In summary, an empirical XANES fit may result in a significant error in yield estimation unless an appropriate reference is used. Successful estimation of NP size and density from absolute-scale EXAFS analysis (Sun *et al.*, 2010) may be due to the validity of the two-component model.

4. Conclusion

Time-resolved *in situ* observation of XAFS spectra provides invaluable information on bond formation kinetics and is extensively studied using synchrotron radiation. Since the technique is dependent on a short-range order, this allows us to investigate the initial stage (nucleation and initial growth) that may not always be crystalline and thus is undetectable by means of spectroscopy which needs a long-range order. In fact, in a large number of studies investigating the mechanism and kinetics of nucleation and growth processes of colloidal NPs, the appearance of absorption or emission features in optical spectra has been conventionally used. Here we show that the combination of *in situ* XAFS and UV–vis absorption provides a feasible way to explore the crystallization process occurring simultaneously with growth, which is, however, difficult using other methods such as HRTEM and *ex situ* XAFS.

The design and performance of a compact *in situ* XAFS apparatus using a microfluidic cell are described. The advantage of a microfluidic cell is its real-time observation capability over a wide range of elapsed time from milliseconds (Chan *et al.*, 2007) to seconds (Uehara *et al.*, 2009). The current design of a reactor cell allows us to record XAFS data within an elapsed time of up to 30 s after initiation of a reaction with a typical flow velocity (8.5 mm s^{-1}). For a much slower reaction a semi-batch experiment (Yao *et al.*, 2010) provides a promising *in situ* technique. Our study on CdSe NPs (Sun *et al.*, 2010) demonstrates that, at the initial stage of the nucleation and growth, Se—Cd bonds are clearly observed with the absence of UV–vis absorption signatures. This suggests that most of the particles in the initial period are in the amorphous state, contrary to hypothesis of the classical nucleation theory. These amorphous nuclei are crystallized rapidly over time, with the rate depending on the reaction conditions such as growth temperature, reaction time, surface ligand and so on. We suggest that the simultaneous crystallization of the existing amorphous particles should be considered for a complete understanding of the growth

mechanism, in particular for NPs synthesized at low temperature or with short reaction time.

References

Alivisatos, A. P. (1996). *J. Phys. Chem.* **100**, 13226–13239.

Ankudinov, A. L., Bouldin, C. E., Rehr, J. J., Sims, J. & Hing, H. (2002). *Phys. Rev. B*, **65**, 104107.

Bowers, M. J., McBride, J. R. & Rosenthal, S. J. (2005). *J. Am. Chem. Soc.* **127**, 15378–15379.

Bullen, C. R. & Mulvaney, P. (2004). *Nano Lett.* **4**, 2303–2307.

Chan, E. M., Marcus, M., Fakara, S., WlNaggar, M., Mathies, R. A. & Alivisatos, A. P. (2007). *J. Phys. Chem. A*, **111**, 12210–12215.

Chen, X. B., Samia, A. C. S., Lou, Y. B. & Burda, C. (2005). *J. Am. Chem. Soc.* **127**, 4372–4375.

Doye, J. P. K. & Calvo, F. (2001). *Phys. Rev. Lett.* **86**, 3570–3573.

Epifani, M., Pellicer, E., Arbiol, J., Sergent, N., Pacnier, T. & Morante, J. R. (2008). *Langmuir*, **24**, 11182–11188.

Geyer, K., Codée, J. D. C. & Seeberger, P. H. (2006). *Chem. Eur. J.* **12**, 8434–8442.

Jose, R., Zhanpeisov, N. U., Fukumura, H., Baba, Y. & Ishikawa, M. (2006). *J. Am. Chem. Soc.* **128**, 629–636.

Kihara, H. (1994). *J. Synchrotron Rad.* **1**, 74–77.

Kudera, S., Zanella, M., Giannini, C., Rizzo, A., Li, Y. Q., Gigli, G., Cingolani, R., Ciccarella, G., Spahl, W., Parak, W. J. & Manna, L. (2007). *Adv. Mater.* **19**, 548–552.

Laaksonen, A., Talanquer, V. & Oxtoby, D. W. (1995). *Annu. Rev. Phys. Chem.* **46**, 489–524.

Leung, K. & Whaley, K. B. (1999). *J. Chem. Phys.* **110**, 11012–11022.

McGinley, C., Riedler, M., Möller, T., Borchert, H., Haubold, S., Haase, M. & Weller, H. (2002). *Phys. Rev. B*, **65**, 245308.

McIlroy, D. N., Zhang, D., Cohen, R. M., Wharton, J., Geng, Y., Norton, M. G., De Stasió, G., Gilbert, B., Perfetti, L., Streiff, J. H., Broocks, B. & McHale, J. L. (1999). *Phys. Rev. B*, **60**, 4874–4879.

Moroni, D., ten Wolde, P. R. & Bolhuis, P. G. (2005). *Phys. Rev. Lett.* **94**, 235703.

Nakamura, H., Tashiro, A., Yamaguchi, Y., Miyazaki, M., Watari, T., Shimizu, H. & Maeda, H. (2004). *Lab. Chip*, **4**, 237–240.

Nakamura, H., Yamaguchi, Y., Miyazaki, M., Maeda, H., Uehara, M. & Mulvaney, P. (2002). *Chem. Commun.* pp. 2844–2845.

Newville, M. (2001). *J. Synchrotron Rad.* **8**, 322–324.

Park, J., Joo, J., Kwon, S. G., Jang, Y. & Hyeon, T. (2007). *Angew. Chem. Int. Ed.* **46**, 4630–4660.

Persans, P. D., Lurio, L. B., Pant, J., Yukselici, H., Lian, G. & Hayes, T. M. (2000). *J. Appl. Phys.* **87**, 3850–3857.

Piepenbrock, M. O. M., Stirner, T., O'Neill, M. & Kelly, S. M. (2007). *J. Am. Chem. Soc.* **129**, 7674–7679.

Ravel, B. & Newville, M. (2005). *J. Synchrotron Rad.* **12**, 537–541.

Rosenthal, S. J., McBride, J., Pennycook, S. J. & Feldman, L. C. (2007). *Surf. Sci. Rep.* **62**, 111–157.

Sahoo, H. R., Kralj, J. G. & Jensen, K. F. (2007). *Angew. Chem. Int. Ed.* **46**, 5704–5708.

Schreuder, M. A., McBride, J. R., Dukes, A. D., Sammons, J. A. & Rosenthal, S. J. (2009). *J. Phys. Chem. C*, **113**, 8169–8176.

Soloviev, V. N., Eichhofer, A., Fenske, D. & Banin, U. (2000). *J. Am. Chem. Soc.* **122**, 2673–2674.

Sun, Z. H., Oyanagi, H., Uehara, M., Nakamura, H., Yamashita, K., Fukano, A. & Maeda, H. (2009). *J. Phys. Chem. C*, **113**, 18608–18613.

Sun, Z. H., Oyanagi, H., Uehara, M., Nakamura, H., Yamashita, K., Fukano, A. & Maeda, H. (2010). *J. Phys. Chem. C*, **114**, 10126–10131.

Tsuruta, H., Nagamura, T., Kimura, K., Igarashi, Y., Kajita, A., Wang, Z.-X., Wakabayashi, K., Amemiya, Y. & Kihara, H. (1989). *Rev. Sci. Instrum.* **60**, 2356–2358.

Uehara, M., Sun, Z. H., Oyanagi, H., Yamashita, K., Fukano, A., Nakamura, H. & Maeda, H. (2009). *Appl. Phys. Lett.* **94**, 063104.

Wang, H. Z., Tashiro, A., Nakamura, H., Uehara, M., Miyazaki, M., Watari, T. & Maeda, H. (2004). *J. Mater. Res.* **19**, 3157–3161.

Xie, C., Hao, H. X., Chen, W. & Wang, J. K. (2008). *J. Cryst. Growth*, **310**, 3504–3507.

Yao, T., Sun, Z., Li, Y., Pan, Z., Wei, H., Xie, Y., Nomura, M., Niwa, Y., Yan, W., Wu, Z., Jiang, Y., Liu, Q. & Wei, S. (2010). *J. Am. Chem. Soc.* **132**, 7696–7701.

Yen, B. K. H., Stott, N. E., Jensen, K. F. & Bawendi, M. G. (2003). *Adv. Mater.* **15**, 1858–1862.

Yoshida, J. (2003). *Microreactors, Epoch-making Technology for Synthesis.* Tokyo: CMC Publishing.

Yu, W. W., Qu, L. H., Guo, W. Z. & Peng, X. G. (2003). *Chem. Mater.* **15**, 2854–2860.

Zhang, J. Y., Wang, X. Y., Xiao, M., Qu, L. & Peng, X. (2002). *Appl. Phys. Lett.* **81**, 2076–2078.

Zhang, T. H. & Liu, X. Y. (2007). *J. Am. Chem. Soc.* **129**, 13520–13526.

Zhang, T. H. & Liu, X. Y. (2009). *Angew. Chem. Int. Ed.* **48**, 1308–1312.

Zhao, Y. H., Lu, K. & Liu, T. (1999). *Phys. Rev. B*, **59**, 11117–11120.